

Origin of magnetocrystalline anisotropy in $(\text{Fe}_{1-x}\text{Co}_x)_2\text{B}$ alloys

Kirill D. Belashchenko,¹ Liqin Ke,² Markus Däne,³ Lorin X. Benedict,³ Tej Nath Lamichhane,^{2,4} Valentin Taufour,^{2,4} Anton Jesche,^{2,4} Sergey L. Bud'ko,^{2,4} Paul C. Canfield,^{2,4} and Vladimir P. Antropov²

¹*Department of Physics and Astronomy and Nebraska Center for Materials and Nanoscience, University of Nebraska-Lincoln, Lincoln, Nebraska 68588, USA*

²*Ames Laboratory, U.S. Department of Energy, Ames, Iowa 50011, USA*

³*Lawrence Livermore National Laboratory, Livermore, California 94550, USA*

⁴*Department of Physics and Astronomy, Iowa State University, Ames, Iowa 50011, USA*

(Dated: January 14, 2015)

Low-temperature measurements of the magnetocrystalline anisotropy energy K in $(\text{Fe}_{1-x}\text{Co}_x)_2\text{B}$ alloys are reported, and the origin of this anisotropy is elucidated using a first-principles electronic structure analysis. The calculated concentration dependence $K(x)$ with a maximum near $x = 0.3$ and a minimum near $x = 0.8$ is in excellent agreement with experiment. This dependence is traced down to spin-orbital selection rules and the filling of electronic bands with increasing electronic concentration. At the optimal Co concentration, K depends strongly on the tetragonality and doubles under a modest 3% increase of the c/a ratio, suggesting that the magnetocrystalline anisotropy can be further enhanced using epitaxial or chemical strain.

Magnetocrystalline anisotropy (MCA) of a magnetic material is one of its key properties for practical applications, large easy-axis anisotropy being favorable for permanent magnets.¹ Intelligent search for new materials requires understanding of the underlying mechanisms of MCA. This is particularly true for substitutional alloys whose properties can be tuned by varying the concentrations of their components. In insulators MCA is often dominated by single-ion terms which can be deduced from crystal-field splittings and spin-orbital (SO) selection rules. In contrast, in typical metals the band width sets the largest energy scale, and the mechanisms of MCA can not be understood without a detailed electronic structure analysis. First-principles calculations are ideally suited for this purpose.

The $(\text{Fe}_{1-x}\text{Co}_x)_2\text{B}$ system²⁻⁶ shows a complicated dependence of the MCA energy K on the concentration. While Fe_2B has a fairly strong easy-plane MCA and Co_2B , at low temperatures, has a small easy-axis MCA, alloying leads to a substantial easy-axis anisotropy around $x = 0.3$,⁵ making this alloy a potentially useful permanent magnet. There is also a deep minimum of K at about $x = 0.8$. The system forms a solid solution at all concentrations.⁵ Therefore, this nonmonotonic variation of K must originate in the continuous evolution of the electronic structure. The main goal of this paper is to elucidate the underlying mechanism of this connection.

First, we report the results of experimental measurements at low temperatures. Single crystals of $(\text{Fe}_{1-x}\text{Co}_x)_2\text{B}$ were grown from solution growth out of an excess of (Fe,Co) which was decanted in a centrifuge.⁷ The single crystals were grown as tetragonal rods which were cut using a wire saw to give them the shape of a rectangular prism. The demagnetization factor was calculated using Ref. 8. Field-dependent magnetization measurements were performed in a Quantum Design MPMS at 2 K in fields up to 5.5 T. The MCA energy K was determined as the area between the two magnetization curves, with the field parallel and perpendicular to the c

axis, taken at the same temperature.⁶ The results shown in Fig. 1 (blue stars) measured at 2 K confirm the non-monotonic concentration dependence, in good agreement with the measurements at 77 K from Ref. 5.

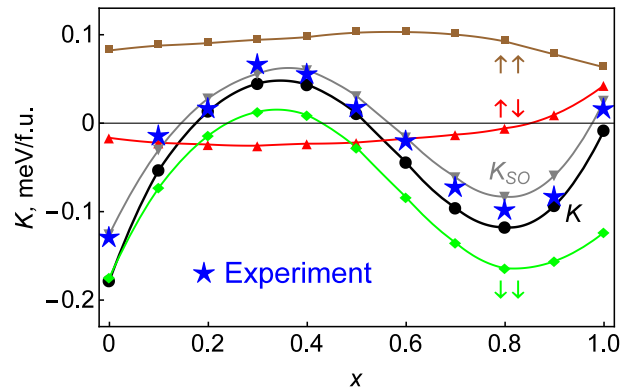


FIG. 1. Calculated (black circles) and experimental (blue stars) MCA energy K in $(\text{Fe}_{1-x}\text{Co}_x)_2\text{B}$ alloys. Gray curve: K_{SO} . The other lines show the spin decomposition $K_{\sigma\sigma'}$.

First-principles calculations were performed using the Green's function-based formulation of the tight-binding linear muffin-tin orbital (GF-LMTO) method⁹ with substitutional disorder treated in the coherent potential approximation (CPA). The SO coupling was included as described in the Appendix. The lattice constants and the internal coordinates are linearly interpolated between the experimental data for the end compounds extrapolated to zero temperature:⁵ $a = 5.109$ and 4.997 Å, $c = 4.249$ and 4.213 Å, and $u = 0.166$ and 0.168 for Fe_2B and Co_2B , respectively. The exchange and correlation are treated within the generalized gradient approximation (GGA).¹⁰ The integration over \mathbf{k} in the calculation of MCA at all concentrations and for both magnetization directions was performed using a uniform mesh of 30^3 points in the full Brillouin zone, which provides sufficient accuracy.

The MCA was found to be sensitive to such computational details as the choice of the exchange-correlation potential and the basis set. This sensitivity is related to the band structure features discussed below, particularly the position of the Fermi level. Our choices result in good agreement with experimental data for all relevant magnetic properties of pure Fe_2B and Co_2B . The calculations at intermediate concentrations were performed without any further concentration-dependent adjustments.

To get the correct MCA at the Co-rich end it is important to have the correct exchange splitting. The experimental²⁻⁶ value of the magnetization in Co_2B is $0.76\mu_B$ per Co atom, while in Fe_2B it is close to $1.9\mu_B$ per Fe atom. The relatively small magnetic moment of Co indicates a pronounced itinerant character of magnetism in Co_2B , which tends to be sensitive to quantum spin fluctuations. Both local spin-density approximation and GGA give an overestimated magnetization of about $1.1\mu_B$ per Co atom. In order to incorporate the effect of spin fluctuations, we introduced a scaling factor for the local part of the effective magnetic field in the GGA functional for the Co atoms and adjusted it to match the experimental magnetization. The resulting scaling factor of 0.80 was then used for Co atoms at all concentrations. The spin moments on different atoms and the total spin magnetization obtained in this way are shown in Fig. 2. While the Fe spin moment is almost constant, the Co spin moment declines with its concentration. Moreover, this decline accelerates at $x \gtrsim 0.6$, which is in excellent agreement with experimental data.²

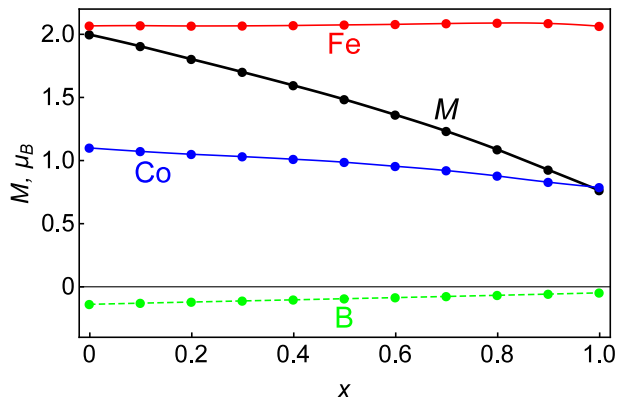


FIG. 2. Spin moments on different atoms and the total spin magnetization M per transition-metal atom. The effective magnetic field for Co atoms is scaled by 0.8 (see text).

Now let us turn to the analysis of MCA. The MCA energy K was obtained by calculating the single-particle energy difference for in-plane and out-of-plane orientations of the magnetization while keeping the LMTO charges fixed at their self-consistent values found without SO coupling. We have verified that the values of K for pure Fe_2B and Co_2B agree very well with Hamiltonian LMTO results. The concentration dependence of K is shown in Fig. 1. The agreement with experimental data

is remarkably good, suggesting that the electronic mechanisms of MCA are correctly captured in the calculations. If the spin moment of Co is not corrected by scaling the exchange-correlation field, the downward trend in K at the Co-rich end continues to large negative values in disagreement with experiment (not shown).

In $3d$ systems the SO band shifts are usually well described by second-order perturbation theory, except perhaps in small regions of the Brillouin zone. Consequently, when MCA appears in second order in SO coupling (as in the tetragonal system under consideration), the anisotropy of the expectation value of the SO operator $\Delta E_{SO} = \langle V_{SO} \rangle_x - \langle V_{SO} \rangle_z$ is approximately equal to $2K$.^{11,12} (Here x or z shows the orientation of the magnetization axis.) We therefore denote $K_{SO} = \Delta E_{SO}/2$ and use the expression $2\langle \mathbf{SL} \rangle = \langle L_{z'} \rangle_{\uparrow\uparrow} - \langle L_{z'} \rangle_{\downarrow\downarrow} + \langle L_+ \rangle_{\downarrow\uparrow} + \langle L_- \rangle_{\uparrow\downarrow}$ to separate the contributions to K by pairs of spin channels. Here we use $L_{z'}$ to denote the component of \mathbf{L} parallel to the magnetization axis, to avoid confusion with the crystallographic z axis; L_{\pm} are the usual linear combinations of the other two (primed) components of \mathbf{L} . The terms $K_{\downarrow\uparrow}$ and $K_{\uparrow\downarrow}$ are identical. The contributions $K_{\sigma\sigma'}$ to K_{SO} are accumulated as energy integrals taking into account the energy dependence of the SO coupling parameters. The results for K_{SO} and $K_{\sigma\sigma'}$ are shown in Fig. 1. First, we see that K_{SO} is close to K , confirming the validity of this analysis. Second, it is clear the non-monotonic concentration dependence is almost entirely due to $K_{\downarrow\downarrow}$. The positive $K_{\uparrow\uparrow}$ term is important, but it depends weakly on x .

It is customary to relate the MCA energy to the orbital moment anisotropy (OMA) ΔM_L .^{1,11,12} Since in the present case both spin channels contribute comparably to K , there is no relation between K and the total OMA. However, since the spin-flip terms are small (see Fig. 1) and the energy dependence of the SO parameters is relatively weak, the contributions $K_{\uparrow\uparrow}$ and $K_{\downarrow\downarrow}$ are closely related to OMA for the states of the corresponding spin. Fig. 3 shows that the concentration-weighted average of the spin-down contribution to OMA behaves similarly to K , while the spin-up contribution is almost constant except for the Co-rich end where, as seen in Fig. 1, the spin-flip terms increase substantially. Note that negative OMA for spin-up states corresponds to positive $K_{\uparrow\uparrow}$, but the sign of OMA for spin-down states is the same as that of $K_{\downarrow\downarrow}$. This is because $\langle L_{z'} \rangle_{\downarrow\downarrow}$ appears in K_{SO} with a minus sign, and it is consistent with Hund's third rule.

Let us now analyze the electronic structure and the details of SO coupling-induced mixing for minority-spin electrons. First, we calculated the minority-spin contribution to K resolved by wave vector \mathbf{k} . For this purpose we calculated the minority-spin spectral function in the presence of SO coupling and found its first energy moment at each \mathbf{k} using an elliptical integration contour in the complex plane. Fig. 4 shows the difference of these integrals for magnetization along the x and z axes, at three key concentrations: pure Fe_2B ($x = 0$), the maximum of K ($x = 0.3$) and its minimum ($x = 0.8$). We have

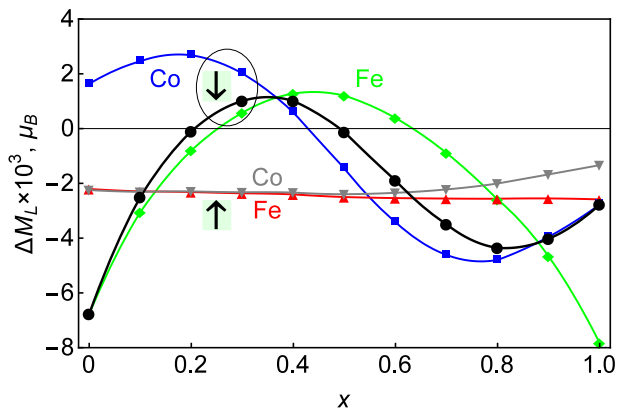


FIG. 3. Orbital moment anisotropy (OMA) for majority and minority-spin states of Fe and Co. The thick black line shows the concentration-weighted average of Fe and Co contributions from the minority-spin states.

checked that the Brillouin zone integral of the \mathbf{k} -resolved MCA energy (summed up over both spins) agrees almost exactly with the value of K calculated in the usual way.

Fig. 4 shows that the MCA energy accumulates over a fairly large part of the Brillouin zone. At $x = 0$ negative contributions to K dominate over most of the Brillouin zone. At $x = 0.3$ both positive and negative contributions are small. At $x = 0.8$ there are regions with large positive and large negative contributions. Overall, it appears that the most important contributions come from the vicinity of the GXM ($k_z = 0$) plane and from the vicinity of the Γ H ($k_x = k_y = 0$) line.

The partial minority-spin spectral functions for the transition-metal site are displayed in Fig. 5 (panels (a)-(c)) along the important high-symmetry directions for the same three concentrations. The coloring in this figure resolves the contributions from different 3d orbitals. At $x = 0$ we have the pure Fe_2B compound and the spectral function resolves the conventional electronic bands (a small imaginary part of 0.004 eV is added to the energy to acquire them). At $x = 0.3$ and $x = 0.8$ substitutional disorder broadens the bands considerably, but their identity is in most cases preserved.

As we have learned above, the dominant concentration dependence of K comes from the $\langle L_{z'} \rangle_{\downarrow\downarrow}$ term, where z' is the magnetization axis. With this in mind, the connection between the character and filling of the electronic bands and MCA can be deduced from the sketch in Fig. 5d, which shows the minority-spin electronic levels appearing at the Γ point at $x = 0$.

The operator \hat{L}_z (relevant for $\mathbf{M} \parallel z$) couples the states corresponding to the same $|m|$, i. e. states of the same color (red or blue) in Fig. 5. The coupling between “red” states is twice stronger, because they correspond to $m = \pm 2$ and “blue” states to $m = \pm 1$. In contrast, \hat{L}_x (relevant for $\mathbf{M} \parallel x$) couples the states m and $m \pm 1$, i. e. “red” states with “blue” states and “blue” states with “green” states. All these couplings contribute to

K only when the Fermi level lies between the two states that are being coupled. Whenever \hat{L}_z or \hat{L}_x couples such states, there is a negative contribution to the energy of the system with the corresponding direction of \mathbf{M} .

The above selection rules remain exact throughout the whole GXM plane, because they are protected by the reflection symmetry $k_z \rightarrow -k_z$. Indeed, “red” and “green” states and \hat{L}_z are even, while “blue” states and \hat{L}_x are odd with respect to this reflection. One consequence of this symmetry is that on this plane “blue” states can not mix with any other states in the absence of SO coupling; this is clearly seen in Fig. 5a.

With the help of Fig. 5 we can now deduce which couplings contribute to K at different concentrations. At $x = 0$ the Fermi level lies between the filled “red” states and empty “blue” states. Coupling of these states by \hat{L}_x contributes to negative K . As the hole pocket centered at Γ is filled with the addition of Co, this contribution is gradually suppressed. At $x = 0.3$ the “blue” band is filled (Fig. 5b), and the minority-spin contribution to K is small (Fig. 4b). These two cases are also indicated in Fig. 5d. As the concentration of Co is further increased, the next “blue” band gets gradually filled, activating the negative contribution to K from the mixing of the filled “blue” and empty “red” states. This trend continues till about $x = 0.8$, where a “red-green” pair of bands (degenerate at Γ) starts to get filled (Fig. 5c). The coupling of these bands by \hat{L}_z leads to an intense positive contribution to K from the vicinity of the Γ point (clearly seen in Fig. 4c), and the trend reverses again. Thus, the non-monotonic dependence of K in the whole concentration range is explained. Note that if the exchange-correlation field on the Co atoms is not scaled down to bring the magnetization in agreement with experiment, the exchange splitting remains too large and the “red-green” bands remain completely empty up to $x = 1$. As a result, without this correction the uninterrupted negative trend brings K to large negative values in disagreement with experiment.

To assess the effect of atomic relaxations on K , we optimized all inequivalent structures with two formula units per unit cell using the VASP code¹³ and the GGA. The volumes were fixed at the same values as in the CPA studies at the same x , while the cell shape and internal coordinates were relaxed. Since all these supercells preserve the σ_z reflection plane, the displacements of Fe and Co atoms are confined to the xy plane. All displacements were less than 0.025 Å. One of the two structures at $x = 0.5$ breaks the C_4 symmetry. For this structure we took the average of the energies for $\mathbf{M} \parallel x$ and $\mathbf{M} \parallel y$ as the in-plane value in the calculation of K , which corresponds to the averaging over different orientations of the same local ordering.

The changes in the absolute value of K due to the relaxation and its values (meV/f.u.) in the relaxed structures were found to be: -26% and -0.11 in Fe_2B , -6% and 0.25 in $\text{Fe}_{1.5}\text{Co}_{0.5}\text{B}$, -13% and 0.15 in the FeCoB [100] superlattice, 6% and 0.12 in the FeCoB [110] superlattice, -11% and -0.31 in $\text{Fe}_{0.5}\text{Co}_{1.5}\text{B}$, and -19%

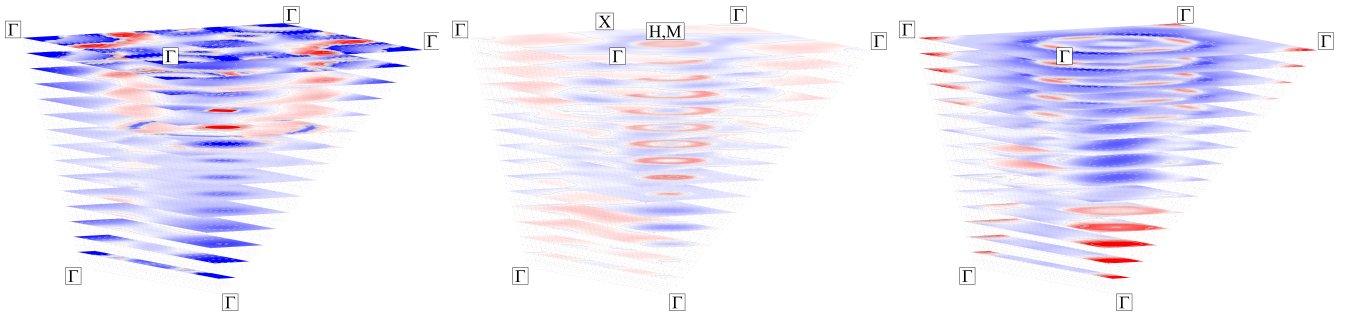


FIG. 4. Brillouin zone map of the k -resolved MCA energy at $x = 0$ (left panel), $x = 0.3$ (middle panel), and $x = 0.8$ (right panel). Half of the Brillouin zone is shown; the top face of the plot is $k_z = 0$. Points H (same as M) and X are shown in the middle panel. The color intensity indicates the magnitude of negative (blue) and positive (red) contributions to K .

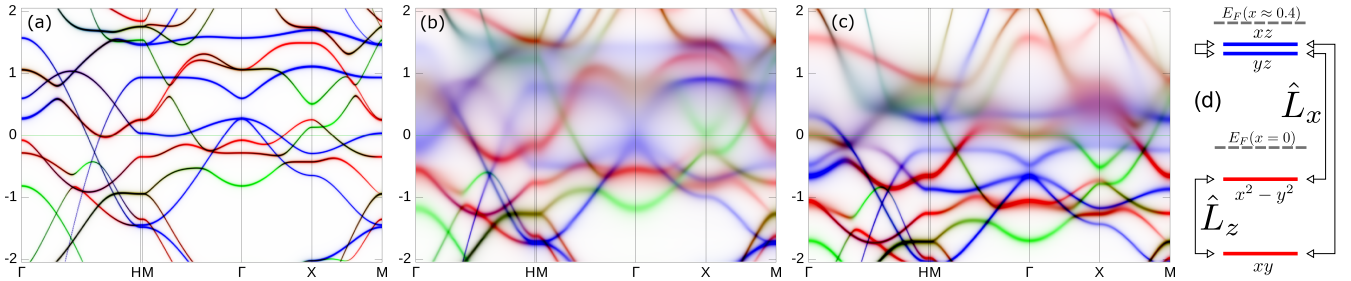


FIG. 5. (a-c) Minority-spin partial spectral functions for the transition-metal site in the absence of SO coupling at (a) $x = 0$, (b) $x = 0.3$, and (c) $x = 0.8$. Energy is in eV. (d) Level diagram and SO selection rules at the Γ point for $x = 0$. Color encodes the orbital character of the states. The intensities of the red, blue and green color channels are proportional to the sum of xy and $x^2 - y^2$ ($m = \pm 2$), sum of xz and yz ($m = \pm 1$), and z^2 ($m = 0$) character, respectively.

and -0.04 in Co_2B . The concentration trend is similar to the CPA results for disordered alloys, although for some ordered structures the values are quite different. Apart from the ordering itself, the difference at the Co-rich end is also due to the use of the spin-fluctuation correction in CPA. Although this set of unit cells is limited, the results suggest that local relaxations do not qualitatively change the concentration dependence shown in Fig. 1.

Larger positive values of K are favorable for permanent magnet applications. Our electronic structure analysis shows that the maximum near $x \approx 0.3$ corresponds to the optimal band filling. Further raising of K requires favorable changes in the band structure, which could be induced by epitaxial or chemical strain. We therefore considered the dependence of K at $x = 0.3$ on the volume-conserving tetragonal distortion. The results plotted in Fig. 6 show a very strong effect: K is doubled under a modest 3% increase in c/a due to the sharply increasing spin-flip contributions. A more detailed analysis shows that the latter is largely due to the increase in the c parameter. On the other hand, the minority-spin contribution increases with decreasing volume. Thus, increasing c and decreasing a both have a positive effect on MCA. This enhancement could be directly utilized through epitaxial multilayer engineering. The search for a suitable alloying element to enhance the c/a ratio is an interesting subject for further investigation.

In conclusion, we have explained how the nonmono-

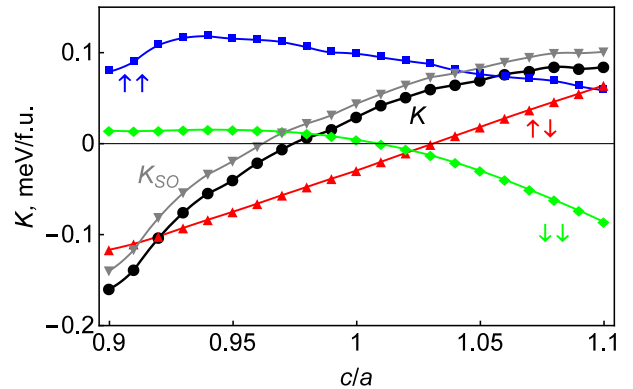


FIG. 6. MCA energy K as a function of the c/a ratio at $x = 0.3$ (the value $c/a = 1$ is assigned to the unstrained lattice). K_{SO} and $K_{\sigma\sigma'}$ are also shown.

tonic concentration dependence of the MCA energy in $(\text{Fe}_{1-x}\text{Co}_x)_2\text{B}$ alloys originates in the consecutive filling of minority-spin electronic bands of particular orbital character and the associated SO selection rules. At the optimal $x = 0.3$ the MCA energy is predicted to increase quickly with the c/a ratio, which could be achieved by epitaxial strain or a suitable chemical doping.

The work at UNL was supported by the National Science Foundation through Grant No. DMR-1308751 and

performed utilizing the Holland Computing Center of the University of Nebraska. Work at Ames Lab and LLNL was supported in part by the Critical Materials Institute, an Energy Innovation Hub funded by the US DOE and by the Office of Basic Energy Science, Division of Materials Science and Engineering. Ames Laboratory is operated for the US DOE by Iowa State University under Contract No. DE-AC02-07CH11358. Lawrence Livermore National Laboratory is operated for the US DOE under Contract DE-AC52-07NA27344.

Appendix: Implementation of spin-orbit coupling in Green's function-based linear muffin-tin orbital (LMTO) method

1. Relation between the Hamiltonian and Green's function-based LMTO formulation

The so-called orthogonal Hamiltonian and Green's function-based LMTO (GF-LMTO) formulations are equivalent to second order in $(E - E_\nu)$ where E_ν is the linearization energy.^{9,14} The Hamiltonian in the orthogonal basis is

$$H_{orth} = C + \sqrt{\Delta}S(1 - \gamma S)^{-1}\sqrt{\Delta}, \quad (\text{A.1})$$

where C , Δ , and γ are the diagonal matrices containing the LMTO potential parameters, and S is the structure constant matrix. On the other hand, in GF-LMTO the Green's function

$$G(z) = \lambda(z) + \mu(z)[P(z) - S]^{-1}\mu(z), \quad (\text{A.2})$$

The third-order term can be treated as a perturbation, and the variational correction formally amounts to the substitution $E\hat{1} \rightarrow E\hat{1} + (E - E_\nu)^3 p$ in the second-order eigenvalue equation $\det(H_{orth} - E) = 0$.

In the GF-LMTO formulation, third-order accuracy is similarly achieved by redefining the potential functions:^{14,15}

$$\tilde{P} = P(\tilde{z}), \quad \tilde{\mu} = \sqrt{\tilde{z}'}\mu(\tilde{z}), \quad \tilde{\lambda} = -\frac{1}{2}\frac{\tilde{z}''}{\tilde{z}'} + \tilde{z}'\lambda(\tilde{z}) \quad (\text{A.7})$$

where $\tilde{z} = z + p(z - E_\nu)^3$ and $\tilde{z}' = d\tilde{z}/dz$. These definitions are designed to preserve the relations (A.4). If the third-order Green's function \tilde{G} is defined similarly to (A.2) but with the third-order potential functions (A.7), it can be shown that

$$\tilde{G} = -\frac{1}{2}\frac{\tilde{z}''}{\tilde{z}'} + \sqrt{\tilde{z}'}(\tilde{z} - H_{orth})^{-1}\sqrt{\tilde{z}'}. \quad (\text{A.8})$$

A solution of $\det(H_{orth} - \tilde{z}) = 0$ corresponds to a pole of \tilde{G} , and the factors $\sqrt{\tilde{z}'}$ guarantee that the residue at

is constructed using the diagonal matrices containing the potential functions

$$P(z) = \frac{z - C}{\Delta_l + \gamma_l(z - C)},$$

$$\mu(z) = \frac{\sqrt{\Delta}}{\Delta + \gamma(z - C)}, \quad \lambda(z) = \frac{\gamma}{\Delta + \gamma(z - C)}. \quad (\text{A.3})$$

These definitions are related through energy derivatives (denoted by an overdot):

$$\mu^2 = \dot{P}, \quad \lambda = -\frac{1}{2}\ddot{P}/\dot{P}. \quad (\text{A.4})$$

These relations guarantee that $G(z)$ does not have poles at the points where $P(z)$ has simple poles. It is straightforward to show that $G(z) = (z - H_{orth})^{-1}$, which means that $G(z)$ in (A.2) is the exact resolvent of H_{orth} .

Third-order parametrization of the potential functions¹⁴ is often considerably more accurate compared to the second-order one. The accuracy of this parametrization is similar to that of the three-center LMTO Hamiltonian, although they are not exactly equivalent. In the nearly orthogonal LMTO basis, the Hamiltonian and overlap matrices are¹⁵

$$H = H_{orth} + (H_{orth} - E_\nu)E_\nu p(H_{orth} - E_\nu),$$

$$O = 1 + (H_{orth} - E_\nu)p(H_{orth} - E_\nu) \quad (\text{A.5})$$

where E_ν and p are diagonal matrices containing the linearization energies and the LMTO parameters $p = \langle \phi^2 \rangle$, and H_{orth} is the same as in (A.1). The generalized eigenvalue problem is then written as

$$\det[(H_{orth} - E) - (H_{orth} - E_\nu)(E - E_\nu)p(H_{orth} - E_\nu)] = 0. \quad (\text{A.6})$$

that pole is equal to 1. Thus, the eigenstates of the three-center LMTO Hamiltonian are correctly represented by \tilde{G} to third order in $E - E_\nu$. The first term in (A.8) introduces two unphysical poles at $z = E_\nu \pm i/\sqrt{3p}$ for each orbital. It is a diagonal matrix which is real on the real axis and has no effect on the spectrum of the physical states.

2. Spin-orbit coupling in GF-LMTO

In the Green's function formalism the perturbation can be introduced through the Dyson equation

$$G_V = G_0 + G_0 \Sigma G_V \quad (\text{A.9})$$

where G_0 and G_V are the unperturbed and perturbed Green's functions and Σ the energy-dependent self-energy due to the perturbation V . For V representing the SO coupling, Σ is local.

In the second-order representation $G_0 = (z - H_{orth})^{-1}$, and therefore $G_V = (z - H_{orth} - \Sigma)^{-1}$. This G_V can be constructed from the potential functions by denoting

$$C_V = C + \Sigma \quad (\text{A.10})$$

and defining the following nondiagonal matrices:

$$\begin{aligned} P_V &= \sqrt{\Delta}[\Delta + (z - C_V)\gamma]^{-1}(z - C_V)\frac{1}{\sqrt{\Delta}} \\ &= [\gamma + \sqrt{\Delta}(z - C_V)^{-1}\sqrt{\Delta}]^{-1} \\ \mu_V^L &= [\Delta + \gamma(z - C_V)]^{-1}\sqrt{\Delta} = (z - C_V)^{-1}\sqrt{\Delta}P_V \\ \mu_V^R &= \sqrt{\Delta}[\Delta + (z - C_V)\gamma]^{-1} = P_V\sqrt{\Delta}(z - C_V)^{-1} \\ \lambda_V &= [\Delta + \gamma(z - C_V)]^{-1}\gamma = \gamma[\Delta + (z - C_V)\gamma]^{-1} \end{aligned} \quad (\text{A.11})$$

The relations (A.4) are then replaced by

$$\dot{P}_V = \mu_V^R \mu_V^L, \quad \lambda_V = -\frac{1}{2}(\mu_V^R)^{-1} \dot{P}(\mu_V^L)^{-1}. \quad (\text{A.12})$$

A tedious but straightforward derivation then shows

$$G_V = \lambda_V + \mu_V^L(P_V - S)^{-1}\mu_V^R. \quad (\text{A.13})$$

If the unperturbed Green's function is calculated to third-order accuracy, we can still proceed from Dyson's equation, but the situation is complicated by the first term $\kappa = -\tilde{z}''/(2\tilde{z}')$ in Eq. (A.8) for \tilde{G}_0 , which modifies the perturbed Green's function \tilde{G}_V . However, for SO coupling this modification may be neglected, as we now argue. Let us denote $\tilde{G}_0 = \kappa + \bar{G}_0$ and write down the diagrammatic expansion of \tilde{G}_V in powers of Σ . It is just a usual expansion in which each Green's function line can be either \bar{G}_0 or κ . Now let us resum all diagram insertions with no external lines and no \bar{G}_0 lines inside. This gives a renormalized self-energy $\bar{\Sigma} = (1 - \Sigma\kappa)^{-1}\Sigma$. Taking this into account and performing the remaining summations, we find

$$\tilde{G}_V = \bar{G} + \kappa + \kappa\bar{\Sigma}\kappa + \kappa\bar{\Sigma}\bar{G} + \bar{G}\bar{\Sigma}\kappa \quad (\text{A.14})$$

where

$$\bar{G} = (1 - \bar{G}_0\bar{\Sigma})^{-1}\bar{G}_0. \quad (\text{A.15})$$

The quantity $\Sigma\kappa \sim p(E - E_\nu)\Sigma$ is very small for SO coupling in transition metals: $\Sigma \sim 50$ meV, $p \sim 0.01$ eV⁻², $E - E_\nu \lesssim 5$ eV. Since κ is analytic on the real axis, $\bar{\Sigma}$ has no poles there too. Therefore, the poles of \tilde{G}_V coincide with the poles of \bar{G} . The latter are just the poles of \bar{G}_0 which are shifted by the self-energy $\bar{\Sigma}$. But $\bar{\Sigma}$ differs from Σ by a factor $(1 - \Sigma\kappa)^{-1}$ which is equal to 1 up to small corrections of order $\Sigma\kappa$. Up to similar corrections, the residues of the poles of \tilde{G}_V are equal to those for \bar{G} . Thus, neglecting all small terms of order $\Sigma\kappa$ compared to 1, we find $\tilde{G}_V \approx \bar{G} + \kappa$.

Substituting the second term in (A.8) as \bar{G}_0 in (A.15), we find the perturbed Green's function:

$$\tilde{G}_V = \sqrt{\tilde{z}'} \left(\tilde{z} - H_{orth} - \sqrt{\tilde{z}'}\Sigma\sqrt{\tilde{z}'} \right)^{-1} \sqrt{\tilde{z}'}. \quad (\text{A.16})$$

where we have dropped the inconsequential term κ . This expression for \tilde{G}_V is equivalent to

$$\tilde{G}_V = \tilde{\lambda}_V + \tilde{\mu}_V^L(\tilde{P}_V - S)^{-1}\tilde{\mu}_V^R \quad (\text{A.17})$$

with redefined potential functions

$$\begin{aligned} \tilde{P}_V &= P_V(\tilde{z}), \quad \tilde{\mu}_V^L = \sqrt{\tilde{z}'}\mu_V^L(\tilde{z}), \\ \tilde{\mu}_V^R &= \mu_V^R(\tilde{z})\sqrt{\tilde{z}'}, \quad \tilde{\lambda}_V = \sqrt{\tilde{z}'}\lambda_V(\tilde{z})\sqrt{\tilde{z}'}, \end{aligned} \quad (\text{A.18})$$

where instead of C_V in (A.10) we should use

$$\tilde{C}_V = C + \sqrt{\tilde{z}'}\Sigma\sqrt{\tilde{z}'}. \quad (\text{A.19})$$

The self-energy matrix for SO coupling within the given l subspace is defined as

$$\Sigma_{SO} = \xi_{l\sigma\sigma'}(z)\langle lm\sigma|\mathbf{SL}|lm'\sigma'\rangle \quad (\text{A.20})$$

where the energy dependence of the coupling parameter $\xi_{l\sigma\sigma'}(z)$ comes from the radial wave functions. To second order in $(z - E_\nu)$, the radial function in the LMTO basis is $\phi_{\nu l\sigma}(z) = \phi_{\nu l\sigma} + (z - E_\nu)\dot{\phi}_{\nu l\sigma}$. Therefore, we have

$$\begin{aligned} \xi_{l\sigma\sigma'}(z) &= \langle \phi_{\nu l\sigma}(z)|V_{SO}(r)|\phi_{\nu l\sigma'}(z)\rangle \\ &= [\langle \phi_{\nu l\sigma}|V_{SO}(r)|\phi_{\nu l\sigma'}\rangle + (z - E_{\nu l\sigma})\langle \dot{\phi}_{\nu l\sigma}|V_{SO}(r)|\phi_{\nu l\sigma'}\rangle + (z - E_{\nu l\sigma'})\langle \phi_{\nu l\sigma}|V_{SO}(r)|\dot{\phi}_{\nu l\sigma'}\rangle \\ &\quad + (z - E_{\nu l\sigma})(z - E_{\nu l\sigma'})\langle \dot{\phi}_{\nu l\sigma}|V_{SO}(r)|\dot{\phi}_{\nu l\sigma'}\rangle] / \sqrt{[1 + p_{l\sigma}(z - E_{\nu l\sigma})^2][1 + p_{l\sigma'}(z - E_{\nu l\sigma'})^2]} \end{aligned} \quad (\text{A.21})$$

where the square roots in the denominator come from the normalization of $\phi_{\nu l\sigma}(z)$.

An approximate form can be obtained by neglecting the terms of order $p(E - E_\nu)^2$ when they appear in the

perturbation, i. e. approximating $\sqrt{\tilde{z}'} \approx 1$ in (A.19) and neglecting the square root in the denominator of (A.21). We found that for $(\text{Fe}_{1-x}\text{Co}_x)_2\text{B}$ alloys this approximation captures all the essential physics (see, for example, Fig. 1), while the $p(E - E_\nu)^2$ terms only change K by an average of about 10%.

The above treatment of SO coupling is extended to the CPA with no modifications. Some implementation notes about our CPA code can be found in Ref. 16.

3. Relation to spin-orbit coupling energy

When magnetocrystalline anisotropy energy K appears in second order in SO coupling, the anisotropy of the expectation value of the SO operator $\Delta E_{SO} = \langle V_{SO} \rangle_x - \langle V_{SO} \rangle_z$ is approximately equal to $2K$.^{11,12} Here we transcribe this relation in terms of Green's functions.

The single-particle energy is by definition

$$E_{sp} = -\frac{1}{\pi} \text{Im Tr} \int z \tilde{G}_V dz \quad (\text{A.22})$$

The second-order term from perturbation theory is

$$\begin{aligned} E_{sp}^{(2)} &= -\frac{1}{\pi} \text{Im Tr} \int z \tilde{G}_0 \Sigma \tilde{G}_0 \Sigma \tilde{G}_0 dz \\ &= -\frac{1}{\pi} \text{Im Tr} \int z \tilde{G}_0^2 \Sigma \tilde{G}_0 \Sigma dz \end{aligned} \quad (\text{A.23})$$

The expectation value of V_{SO} , with the radial integral included in Σ , in the same order is

$$\langle V_{SO} \rangle = -\frac{1}{\pi} \text{Im Tr} \int \Sigma \tilde{G} dz \approx -\frac{1}{\pi} \text{Tr} \int \Sigma \tilde{G}_0 \Sigma \tilde{G}_0 dz. \quad (\text{A.24})$$

An exact quasiparticle Green's function with simple poles of unit residue satisfies $dG/dz = -G^2$. For \tilde{G}_0 this identity is satisfied approximately up to a real term of second order in $(E - E_\nu)$. Thus, setting $d\tilde{G}_0/dz \approx -\tilde{G}_0^2$, we find

$$\begin{aligned} E_{sp}^{(2)} &\approx \frac{1}{\pi} \text{Im Tr} \int z \frac{1}{2} \frac{d}{dz} (\tilde{G}_0 \Sigma \tilde{G}_0 \Sigma) dz + ((d\Sigma/dz)) \\ &= \frac{\langle V_{SO} \rangle}{2} + ((d\Sigma/dz)) \end{aligned} \quad (\text{A.25})$$

where the first term was integrated by parts, and $((d\Sigma/dz))$ denotes the terms with the energy derivative of Σ . For substitutional alloys treated in CPA, the Green's function does not have a purely quasiparticle structure, and in general the relation $dG/dz = -G^2$ is violated due to the energy dependence of the coherent potential. This energy dependence contributes additional terms to the right side of (A.25). However, here we are dealing with relatively weak substitutional Fe/Co disorder, and the electronic structure largely preserves its quasiparticle character. Therefore, we may expect the relation $E_{sp}^{(2)} \approx \langle V_{SO} \rangle/2$ to hold approximately, which is borne out by calculations. Deviations from this relation can also occur near the points of degeneracy close to the Fermi level, where second-order perturbation theory breaks down. As seen in Fig. 4, this situation appears near $x = 0.8$ where the Fermi level cuts through a pair of flat, nearly degenerate bands. From Fig. 1 we see the largest difference between K and K_{SO} at this point.

¹ J. Stohr and H. Siegmann, in *Magnetism: From fundamentals to Nanoscale Dynamics* (Springer, Berlin, 2006), p. 805.
² M. C. Cadeville and I. Vincze, *J. Phys.: Metal Phys.* **5**, 790 (1975).
³ L. Takacs, M. C. Cadeville, and I. Vincze, *J. Phys. F: Metal Phys.* **5**, 800 (1975).
⁴ W. Coene, F. Hakkens, R. Coehoorn, D. B. de Mooij, C. de Waard, J. Fidler and R. Grössinger, *J. Magn. Magn. Mater.* **96**, 189 (1991).
⁵ A. Iga, *Jpn. J. Appl. Phys.* **9**, 415 (1970).
⁶ M. D. Kuz'min, K. P. Skokov, H. Jian, I. Radulov and O. Gutfleisch, *J. Phys.: Condens. Matter* **26**, 064205 (2014).
⁷ P. C. Canfield and Z. Fisk, *Philos. Mag.* **B 65**, 1117 (1992).
⁸ A. Aharoni, *J. Appl. Phys.* **83**, 3432 (1998).
⁹ I. Turek, V. Drchal, J. Kudrnovský, M. Šob, and P. Wein-

berger, *Electronic structure of disordered alloys, surfaces and interfaces* (Kluwer, Boston, 1997).
¹⁰ J. P. Perdew, K. Burke, and M. Ernzerhof, *Phys. Rev. Lett.* **77**, 3865 (1996); **78**, 1396 (1997).
¹¹ V. P. Antropov, L. Ke, and D. Aberg, *Solid State Commun.* **194**, 35 (2014).
¹² V. P. Antropov and V. N. Antonov, *Phys. Rev. B* **90**, 094406 (2014).
¹³ G. Kresse and J. Furthmüller, *Comput. Mat. Sci.* **6**, 15 (1996).
¹⁴ O. Gunnarsson, O. Jepsen, and O. K. Andersen, *Phys. Rev. B* **27**, 7144 (1983).
¹⁵ O. K. Andersen, O. Jepsen, and D. Glötzel, in *Highlights of Consensed-Matter Theory*, ed. F. Bassani, F. Fumi, and M. P. Tosi (North-Holland, Amsterdam, 1985).
¹⁶ L. Ke, K. D. Belashchenko, M. van Schilfgaarde, T. Kotani, and V. P. Antropov, *Phys. Rev. B* **88**, 024404 (2013).